Noname manuscript No.
(will be inserted by the editor)

Mechanistic analysis of rock damage anisotropy and rotation around circular cavities

Hao Xu · Chloé Arson

Received: date / Accepted: date

Abstract We used the Differential Stress Induced Damage (DSID) model to predict anisotropic crack propagation under tensile and shear stress. The damage variable is similar to a crack density tensor. The damage function and the damage potential are expressed as functions of the energy release rate, defined as the thermodynamic force that is work-conjugate to damage. Contrary to previous damage models, flow rules are obtained by deriving dissipation functions by the energy release rate, and thermodynamic consistency is ensured. The damage criterion is adapted from the Drucker-Prager yield function. Simulations of biaxial stress tests showed that: (1) three dimensional states of damage can be obtained

Hao Xu

School of Civil and Environmental Engineering, Georgia Institute of Technology, Atlanta, Georgia.

E-mail: haoxu@gatech.edu

Chloé Arson

School of Civil and Environmental Engineering, Georgia Institute of Technology, Atlanta, Georgia.

E-mail: chloe.arson@ce.gatech.edu

for three dimensional states of stress; (2) no damage propagates under isotropic compression; (3) crack planes propagate in the direction parallel to major compression stress; (4) damage propagation hardens the material; (5) stiffness and deformation anisotropy result from the anisotropy of damage. There is no one-to-one relationship between stress and damage. We demonstrated the effect of the loading sequence in a two-step simulation (a shear loading phase and a compression loading phase): the current state of stress and damage can be used to track the effect of stress history on damage rotation. We finally conducted a sensitivity analysis with the Finite Element Method, to explore the stress conditions in which damage is expected to rotate around a circular cavity subject to pressurization or depressurization. Simulation results showed that: (1) before damage initiation, the DSID model matches the analytical solution of stress distribution obtained with the theory of elasticity; (2) the DSID model can predict the extent of the tensile damage zone at the crown, and that of the compressive damage zone at the sidewalls; (3) damage generated during a vertical far field compression followed by a depressurization of the cavity is more intense than that generated during a depressurization of the cavity followed by a vertical far-field compression.

Keywords rock mechanics · Continuum Damage Mechanics · thermodynamics · Finite Element Method · damage rotation · anisotropy · circular cavity

1 Introduction

This study aims to provide a rigorous modeling approach to predict anisotropic damage in rock engineering problems. Continuum Damage Mechanics (CDM) enables predicting the stress-path dependence of elastic properties in cracked solids

(Krajcinovic, 1996; Lemaître and Desmorat, 2005). CDM was extended to heterogeneous materials such as concrete (Lee and Fenves, 1998; Lubliner et al, 1989; Mazars, 1986; Mazars and Pijaudier-Cabot, 1989) and rock (Arson, 2012; Halm and Dragon, 1998; Homand-Etienne et al, 1998; Shao et al, 2005; Zhu and Arson, 2014). Damage is defined as a fabric tensor, which describes the geometry of discontinuities of geological objects (e.g., joints, faults) in terms of position and density, shape, dimension and orientation (Oda, 1982). CDM avoids modelling all cracks at the micro-scale - as opposed to micro-mechanics: damage effects are analyzed at the scale of a Representative Elementary Volume Element (REV), which makes it well-suited for numerical implementation in Finite Element Methods (FEM); discontinuities are modeled as energy losses at the scale of the continuum REV (Gatmiri and Arson, 2008).

The main inconvenience of CDM is that there is no one-to-one relationship between damage and the pattern of micro-cracks; a rotation of the principal directions of the damage tensor can correspond to several micro-mechanisms, including microscopic shear or bifurcation of tensile stress. Damage rotation can be modeled numerically, by updating the principal base of damage at each load step (Halm and Dragon, 1998). Theoretical models of continuum damage rotation require microstructure descriptors or complementary dissipation potentials. Specifically, damage rotation is modeled as a mixed mode crack propagation, which is captured by splitting damage into volumetric and deviatoric components (Hou, 2003; Lux and Eberth, 2007; Hunsche and Hampel, 1999), or by relating several rate-dependent scalar damage variables to independent creep mechanisms (Chan et al, 1996, 2001; Zhou et al, 2011; Raj, 1982; Carter and Hansen, 1983; Senseny et al, 1992). In (Abu Al-Rub and Kim, 2010; Chaboche, 1992, 1993; Frémond and

Nedjar, 1996), several damage thresholds are employed to distinguish damage in tension and damage in compression, and to model the effects of crack closure on the damaged stiffness tensor. In such approaches, shear damage is in fact driven by differential stress; tensile micro-cracks linked together by wing cracks are represented as macroscopic "composite" flaws (Deng and Nemat-Nasser, 1992; Swoboda and Yang, 1999; Huang et al, 2002; Chan et al, 1996; Horii and Nemat-Nasser, 1986; Nemat-Nasser and Hori, 1983; Ashby and Sammis, 1990).

In this paper, we model crack-induced anisotropy in quasi-brittle geomaterials subject to different failure criteria in tension and compression. The goal is to analyze the microscopic and macroscopic mechanisms driving the rotation of the principal directions of damage. We used the FEM to simulate various stress paths with the Differential Stress-Induced Damage (DSID) model previously proposed by the authors (Xu and Arson, 2014). The damage variable is similar to a crack density tensor. Damage represents three equivalent macroscopic cracks (defined at the scale of the REV); damage eigenvectors are orthogonal to the macroscopic crack planes, and damage eigenvalues are the volume fractions of these macroscopic cracks. The damage criterion is similar to the Drucker-Prager yield function, except that the criterion is expressed in terms of damage energy release rate projected in the positive space, in order to distinguish between tension and compression damage thresholds. Section 2 explains the mathematical and physical meaning of the energy potentials introduced in the formulation, and summarizes the assumptions made in the model. Section 3 discusses damage anisotropy obtained under biaxial stress states. Section 4 explains how the rotation of the damage tensor relates to microscopic and macroscopic stress changes, and how the DSID model can be used to infer the distribution of several crack types from phenomenological predictions

of stress and damage. Finite Element (FE) analyses of anisotropic stress and damage distributions around a circular cavity are presented in Sections 5 and 6. The boundaries of the domain allow one to study several configurations of stress, in which anisotropy is either part of the reference state or induced by the imposed stress.

2 Outline of the Differential Stress Induced Damage (DSID) Model

2.1 Thermodynamic Framework

The damage variable used in the Differential Stress-Induced Damage (DSID) model (Xu and Arson, 2014) is a second-order tensor, expressed as

$$\boldsymbol{\Omega} = \sum_{k=1}^{N} d_k \mathbf{n}_k \otimes \mathbf{n}_k \tag{1}$$

in which the Representative Elementary Volume Element (REV) is assumed to contain N cracks characterized by a normal direction $\boldsymbol{n}_k$ and a volumetric fraction d_k (Figure 1). The damage variable defined in Equation 1 is similar to Kachanov's crack density tensor (Kachanov, 1992) and Oda's fabric tensor (Oda, 1984).

In order to account for residual crack openings induced by damage (Abu Al-Rub and Voyiadjis, 2003), the deformation tensor is decomposed as

$$\boldsymbol{\varepsilon} = \boldsymbol{\varepsilon}^{el} + \boldsymbol{\varepsilon}^{ed} + \boldsymbol{\varepsilon}^{id} = \boldsymbol{\varepsilon}^{E} + \boldsymbol{\varepsilon}^{id} \tag{2}$$

in which $\boldsymbol{\varepsilon}^{el}$ is the purely elastic deformation, $\boldsymbol{\varepsilon}^{ed}$ is the elastic damage-induced deformation due to the degradation of mechanical stiffness, and $\boldsymbol{\varepsilon}^{id}$ is the irreversible deformation tensor. $\boldsymbol{\varepsilon}^{E}$ is the total elastic deformation. Dissipation (Φ_s) is assumed to depend on inelastic strains $\boldsymbol{\varepsilon}^{id}$ and damage $\boldsymbol{\Omega}$ only (Hansen and

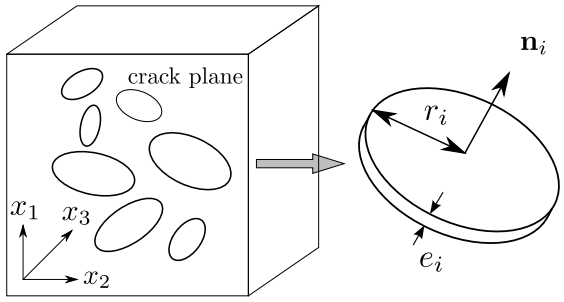

Fig. 1 Representation of Oda's Fabric Tensor. Each of the crack plane is assumed to be penny-shaped, with a radius r_i and a thickness e_i. The plane direction of the i-th crack is given by the normal vector $\mathbf{n}_i$. The Fabric Tensor can be obtained by projecting all crack planes into three principal directions, x_i. Modified from Oda (1984, 1982); Arson (2009); Xu (2014)

Schreyer, 1994; Houlsby and Puzrin, 2006; Yu, 2006). In the absence of additional hardening variable, the positivity of the dissipation potential is automatically satisfied if

$$\boldsymbol{\sigma} : \dot{\boldsymbol{\varepsilon}}^{id} \geq 0, \qquad \mathbf{Y} : \dot{\boldsymbol{\Omega}} \geq 0 \tag{3}$$

in which $\boldsymbol{\sigma}$ and $\mathbf{Y}$ are respectively the stress variable and the energy release rate variable. $\mathbf{Y}$ is the thermodynamic force that is work-conjugate to damage: it is obtained by deriving the free energy by damage (as explained in the following section). The fundamental principles of thermodynamics used to derive the DSID constitutive relationships are explained in detail e.g. by (Collins and Houlsby, 1997; Houlsby and Puzrin, 2006; Desmorat, 2006; Hütter and Tervoort, 2008; Keller and Hutter, 2011; Voyiadjis et al, 2011). Three functionals are needed for the model formulation: (1) *the skeleton free energy* (for instance, Gibbs free energy G_s), (2) *a damage criterion* f_d, and (3) *a dissipation potential* g_d (to derive the evolution laws of internal variables considered in the model). Details on the postulates made to derive the closed set of constitutive equations are provided in the following section.

2.2 The Three Thermodynamic Functionals in the DSID Model

2.2.1 Free Energy of the Solid Skeleton

Damaged stress-strain relationships can be derived from Helmholtz free energy (Abu Al-Rub and Kim, 2010; Cicekli et al, 2007; Murakami and Kamiya, 1996) or from Gibbs free energy (Halm and Dragon, 1998; Homand-Etienne et al, 1998; Chaboche, 1993; Pellet et al, 2005). In order to facilitate the calibration of parameters against experimental data, the DSID model was formulated in terms of Gibbs free energy, because elastic strains cannot be controlled as such in an experiment or in a numerical simulation. The expression of Gibbs free energy was chosen according to the approach proposed in Shao et al (2005, 2006) and Zhou et al (2006):

$$\begin{aligned} G_s\left(\boldsymbol{\sigma},\boldsymbol{\Omega}\right) = \frac{1}{2}\boldsymbol{\sigma}:\mathbb{S}_0:\boldsymbol{\sigma} + a_1 \mathrm{tr}\boldsymbol{\Omega}\left(\mathrm{tr}\boldsymbol{\sigma}\right)^2 + a_2 \mathrm{tr}(\boldsymbol{\sigma}\cdot\boldsymbol{\sigma}\cdot\boldsymbol{\Omega}) \\ + a_3 \mathrm{tr}\boldsymbol{\sigma}\,\mathrm{tr}(\boldsymbol{\Omega}\cdot\boldsymbol{\sigma}) + a_4 \mathrm{tr}\boldsymbol{\Omega}\,\mathrm{tr}(\boldsymbol{\sigma}\cdot\boldsymbol{\sigma}) \end{aligned} \tag{4}$$

in which $\mathbb{S}_0$ is the compliance of the intact material, in the absence of damage; a_1, a_2, a_3 and a_4 were initially introduced in the free energy to capture the increase of rock compliance with damage growth (Hayakawa and Murakami, 1997) and were then related to consequent microstructure changes (Shao et al, 2005). a_1 is a scaling parameter, which is used to model damage produced under hydrostatic stress (Bakhtiary et al, 2014). a_2 and a_4 control rock behavior under deviatoric stress. a_3 accounts for the deviation of stress from the principal directions of damage. In the absence of damage, we assume that the material has a linear elastic behavior; therefore, the terms of the free energy that depend on stress are at most quadratic (Halm and Dragon, 1998; Shao et al, 2005). The stress-strain relationship is ob-

tained by deriving Gibbs free energy:

$$\begin{aligned}\boldsymbol{\varepsilon}^E = \boldsymbol{\varepsilon} - \boldsymbol{\varepsilon}^{id}(\boldsymbol{\Omega}) = \frac{\partial G_s}{\partial \boldsymbol{\sigma}} = \frac{1+\nu_0}{E_0}\boldsymbol{\sigma} - \frac{\nu_0}{E_0}(\mathrm{tr}\boldsymbol{\sigma})\,\boldsymbol{\delta} + 2a_1(\mathrm{tr}\boldsymbol{\Omega}\,\mathrm{tr}\boldsymbol{\sigma})\,\boldsymbol{\delta} \\ + a_2(\boldsymbol{\sigma}\cdot\boldsymbol{\Omega} + \boldsymbol{\Omega}\cdot\boldsymbol{\sigma}) + a_3[\,\mathrm{tr}(\boldsymbol{\sigma}\cdot\boldsymbol{\Omega})\,\boldsymbol{\delta} + (\mathrm{tr}\boldsymbol{\sigma})\,\boldsymbol{\Omega}\,] + 2a_4(\mathrm{tr}\boldsymbol{\Omega})\,\boldsymbol{\sigma}\end{aligned} \tag{5}$$

where $\boldsymbol{\delta}$ is the second-order identity tensor, and E_0 and ν_0 are Young's modulus and Poisson's ratio of the intact material. Similarly the damage driving force is:

$$\mathbf{Y} = \frac{\partial G_s}{\partial \boldsymbol{\Omega}} = a_1(\mathrm{tr}\boldsymbol{\sigma})^2\,\boldsymbol{\delta} + a_2\boldsymbol{\sigma}\cdot\boldsymbol{\sigma} + a_3\mathrm{tr}(\boldsymbol{\sigma})\boldsymbol{\sigma} + a_4\mathrm{tr}(\boldsymbol{\sigma}\cdot\boldsymbol{\sigma})\boldsymbol{\delta} \tag{6}$$

Model parameters can be obtained by inverting the constitutive relationships obtained from stress-strain curves (Halm and Dragon, 2002; Hayakawa and Murakami, 1997).

2.2.2 Damage Function

The DSID model is designed to predict damage induced by gradients of stress differences. We used a damage criterion similar to the Drucker-Prager yield function. The left-hand side plot in Figure 2 shows that the damage surface obtained by substituting stress by the damage-driving force (Equation 6) in the Drucker-Prager yield function is made of eight connected, identical, truncated cones. As the figure illustrates, the damage criterion based on the Drucker-Prager function implies that the material has the same strength under pure compression loading and under pure tension loading, which is not realistic for rock materials. In order to overcome this limitation, we expressed the damage function in terms of a "physical damage-driving force $\mathbb{P}_1 : \mathbf{Y}$, calculated by projecting the damage-driving force $\mathbf{Y}$ with the following fourth-order operator:

$$\mathbb{P}_1(\boldsymbol{\sigma}) = \sum_{p=1}^{3}\left[H(\sigma^{(p)}) - H(-\sigma^{(p)})\right]\mathbf{n}^{(p)}\otimes\mathbf{n}^{(p)}\otimes\mathbf{n}^{(p)}\otimes\mathbf{n}^{(p)} \tag{7}$$

$H(\cdot)$ is the Heaviside distribution function, $\sigma^{(p)}$ is the p^{th} eigenstress value, and $\mathbf{n}^{(p)}$ is the vector aligned with the p^{th} principal direction of stress. We defined the damage function as follows:

$$f_d = \sqrt{J^*} - \alpha I^* - (C_0 + C_1 \mathrm{Tr}\,(\boldsymbol{\Omega})) \tag{8}$$

C_0 is the initial damage threshold; C_1 is a damage hardening variable (Halm and Dragon, 1998); and α is a parameter controlling the shape of the damage surface, similar to the parameter controlling the angle of the 3D cone that represents the yield surface in the Drucker-Prager plasticity model. J^* and I^* are defined as

$$J^* = \frac{1}{2}(\mathbb{P}_1 : \mathbf{Y} - \frac{1}{3} I^* \boldsymbol{\delta}) : (\mathbb{P}_1 : \mathbf{Y} - \frac{1}{3} I^* \boldsymbol{\delta}), \quad I^* = (\mathbb{P}_1 : \mathbf{Y}) : \boldsymbol{\delta} \tag{9}$$

In $\mathbb{P}_1 : \mathbf{Y}$ space, the damage surface is a cone - similar to Drucker-Prager yield surface (Figure 3(a)). Amongst the eight cones that produce the damage surface in the absence of projection, only the cone that corresponds to purely compressive stress states remains in the modified damage surface (represented in red in the left-hand side plot of Figure 2). This cone is connected to a closed surface that represents the strength of the material when at least one of the eigenstresses is tension (negative values): as shown in the right-hand side plot of Figure 2, the modified damage surface clearly distinguishes tensile and compressive strengths. The projection tensor $\mathbb{P}_1$ ensures that the occurrence of damage is controlled by the action of the damage driving force in the stress principal directions, and that in each stress principal direction, the eigenvalues of the physical damage driving force $(\mathbb{P}_1 : \mathbf{Y})$ is of the same sign as the differential stress eigenvalues.

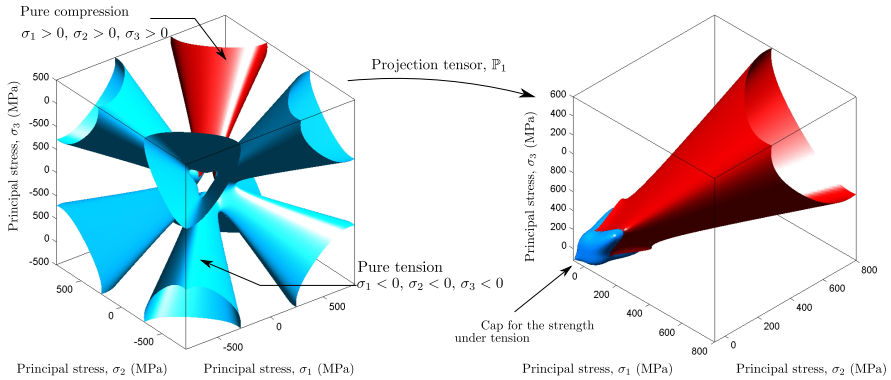

Fig. 2 Left: Surface of the damage criterion if stress is replaced by the damage-driving force $\mathbf{Y}$ (eight identical cones) in the Drucker-Prager yield function. Right: Surface of the damage criterion if stress is replaced by the physical damage-driving force $\mathbb{P}_1 : \mathbf{Y}$ in the Drucker-Prager yield function: The part in red represents compression strength and the part in light green represents the strength in states of stress in which at least one eigenstress is a tension.

2.2.3 Damage Potential

In CDM, the positivity of dissipation is automatically ensured if the damage rate is positive (Desmorat, 2006). As shown in (Xu and Arson, 2014), the damage rate in the DSID model is not unconditionally positive if the damage flow rule is associate (because of the term αI^*). In order to ensure the positivity of dissipation, we adopted a non-associate damage rule:

$$\dot{\boldsymbol{\Omega}} = \dot{\lambda}_d \frac{\partial g_d}{\partial \mathbf{Y}} \tag{10}$$

In which the damage potential is written as

$$g_d = \sqrt{\frac{1}{2}(\mathbb{P}_2 : \mathbf{Y}) : (\mathbb{P}_2 : \mathbf{Y})} - C_2 \tag{11}$$

The definition of the projection tensor $\mathbb{P}_2$ allows one to model the propagation of mode I cracks under tension, and wing cracks under compression:

$$\mathbb{P}_2 = \sum_{p=1}^{3} H\left[\max_{q=1}^{3}(\sigma^{(q)}) - \sigma^{(p)}\right] \mathbf{n}^{(p)} \otimes \mathbf{n}^{(p)} \otimes \mathbf{n}^{(p)} \otimes \mathbf{n}^{(p)} \tag{12}$$

Table 1 illustrates the propagation of damage under various stress conditions. Note that we considered $\sigma_{11} \geq \sigma_{22} > \sigma_{33}$, with σ_{11} the stress parallel to the vertical direction.

It is possible to calibrate the material parameters a_i in order to ensure the positivity of the components of $\frac{\partial g_d}{\partial \mathbf{Y}}$ (Xu, 2014). The positivity of $\frac{\partial g_d}{\partial \mathbf{Y}}$ ensures the positivity of the damage rate, and therefore, the thermodynamic consistency of the model. Figure 3(a) shows the shape of the damage surface, and Figure 3(b) shows the shape of the damage potential. Hardening occurs when damage cumulates: the domain inside the damage yield surface and inside the potential surface expand.

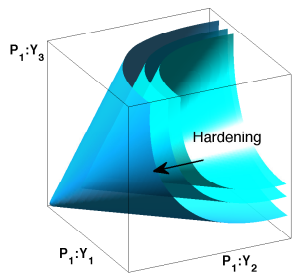

(a) Damage function in the space of physical damage driving force $\mathbb{P}_1 : \boldsymbol{Y}$

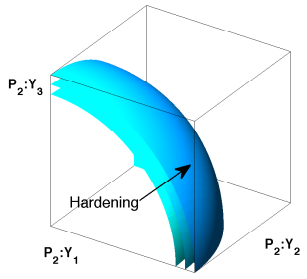

(b) Damage potential in the space of physical damage driving force $\mathbb{P}_2 : \boldsymbol{Y}$

Fig. 3 Damage surface and damage potential in the DSID model.

If the rate of irreversible deformation is derived from the damage potential defined in Equation 11, it can be shown that the principal directions of the irreversible strain rate are equal to the stress principal directions, and that in each

Table 1 Damage propagation under various stress conditions: the direction of the damage rate is defined by the projection tensor $\mathbb{P}_2$.

Case	sketch	Damage
Uniaxial compression $\sigma_{11} > 0$ $\sigma_{22} = \sigma_{33} = 0$	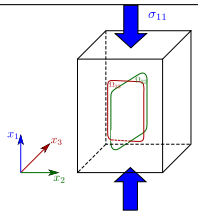	$\begin{bmatrix} 0 & 0 & 0 \\ 0 & \Omega_{22} & 0 \\ 0 & 0 & \Omega_{33} \end{bmatrix}$
Uniaxial tension $\sigma_{11} = \sigma_{22} = 0$ $\sigma_{33} < 0$	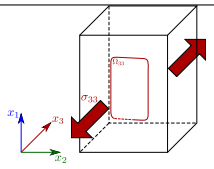	$\begin{bmatrix} 0 & 0 & 0 \\ 0 & 0 & 0 \\ 0 & 0 & \Omega_{33} \end{bmatrix}$
Triaxial compression $\sigma_{11} > \sigma_{22} = \sigma_{33} > 0$	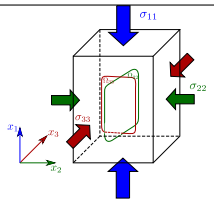	$\begin{bmatrix} 0 & 0 & 0 \\ 0 & \Omega_{22} & 0 \\ 0 & 0 & \Omega_{33} \end{bmatrix}$
Biaxial compression $\sigma_{11} = \sigma_{22} > 0$ $\sigma_{33} = 0$	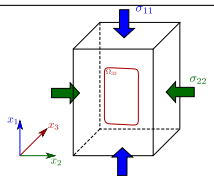	$\begin{bmatrix} 0 & 0 & 0 \\ 0 & 0 & 0 \\ 0 & 0 & \Omega_{33} \end{bmatrix}$
Biaxial compression-tension $\sigma_{11} > \sigma_{22} > 0$ $\sigma_{33} < 0$	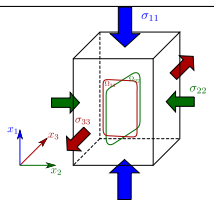	$\begin{bmatrix} 0 & 0 & 0 \\ 0 & \Omega_{22} & 0 \\ 0 & 0 & \Omega_{33} \end{bmatrix}$

principal direction, the rate of irreversible strains has the same sign as the stress rate (Xu and Arson, 2014). In order to ensure that irreversible deformation propagates in planes normal to the major principal stress direction, an associate flow rule is used for the rate of irreversible deformation:

$$\dot{\boldsymbol{\varepsilon}}^{id} = \dot{\lambda}_d \frac{\partial f_d}{\partial \boldsymbol{\sigma}} = \dot{\lambda}_d \frac{\partial f_d}{\partial \mathbf{Y}} \frac{\partial \mathbf{Y}}{\partial \boldsymbol{\sigma}} \tag{13}$$

with

$$\frac{\partial f_d}{\partial \boldsymbol{\Omega}} = -C_1\boldsymbol{\delta}; \quad \frac{\partial g}{\partial \mathbf{Y}} = \frac{(\mathbb{P}_2:\mathbf{Y}):\mathbb{P}_2}{\sqrt{2(\mathbb{P}_2:\mathbf{Y}):(\mathbb{P}_2:\mathbf{Y})}}$$

$$\frac{\partial f_d}{\partial \mathbf{Y}} = \frac{\left[\mathbb{P}_1:\mathbf{Y}-\frac{1}{3}(\boldsymbol{\delta}:\mathbb{P}_1:\mathbf{Y})\boldsymbol{\delta}\right]:\left[\mathbb{P}_1-\frac{1}{3}\boldsymbol{\delta}\otimes(\boldsymbol{\delta}:\mathbb{P}_1)\right]}{\sqrt{2\left[\mathbb{P}_1:\mathbf{Y}-\frac{1}{3}(\boldsymbol{\delta}:\mathbb{P}_1:\mathbf{Y})\boldsymbol{\delta}\right]\left[\mathbb{P}_1:\mathbf{Y}-\frac{1}{3}(\boldsymbol{\delta}:\mathbb{P}_1:\mathbf{Y})\boldsymbol{\delta}\right]}} - \alpha\boldsymbol{\delta}:\mathbb{P}_1 \tag{14}$$

3 Stress and damage evolution during biaxial compression tests

We simulated a series of biaxial compression tests at the material point level. Stress in one of the horizontal direction was zero: $\sigma_{33} = 0$, and we studied the evolution of stress and damage for different stress ratios: $K_p = \frac{\sigma_h}{\sigma_v} = \frac{\sigma_{22}}{\sigma_{11}} = 0 \sim 2$, in which direction 1 refers to the vertical. These states of stress occur when the rock mass is subject to a deconfinement, as is the case at the wall of a cavity, where stress in one of the directions of space is zero (i.e. $\sigma_{rr} = \sigma_{33} = 0$). When $K_p < 1$, the horizontal stress (e.g. σ_{22}) is less than the vertical stress. $K_p > 1$ indicates that the horizontal stress exceeds the vertical stress. In the following, we fixed the value of the vertical stress σ_{11} to 200 MPa - which can be considered as a study of the influence of horizontal stresses on damage evolution at constant depth in field conditions. The simulations were performed under controlled stress conditions, with a biaxial confinement stage followed by a deviatoric loading stage: for $K_p > 1$, we used $\sigma_{11} = \sigma_{22} = 200$ MPa in the confining stage and we then increased σ_{22} under $\sigma_{11} = 200$ MPa during the deviatoric loading stage; for $K_p < 1$, we first applied $\sigma_{11} = \sigma_{22} = \sigma_h < 200$ MPa during the confining phase, and we then applied a vertical stress equal to $\sigma_{11} = 200\,\text{MPa} - \sigma_h$ under $\sigma_{22} = \sigma_h$ during the deviatoric loading stage.

Figure 4 shows the final values of the accumulated damage components at the end of the compression tests. Results indicate that:

- When $K_p < 1$, Ω_{22} and Ω_{33} propagate during the deviatoric loading stage. Physically, this state of damage corresponds to a set of vertical cracks. Horizontal cracks do not propagate, therefore $\Omega_{11} = 0$.
- When $K_p > 1$, σ_{22} is the maximum principal compressive stress, therefore damage components Ω_{11} (horizontal cracks) and Ω_{33} (vertical cracks) propagate during the deviatoric loading stage. Physically, this state of damage is produced by the differential stresses $\sigma_{22} - \sigma_{11}$ and $\sigma_{22} - \sigma_{33}$. Vertical crack planes normal to the maximum stress σ_{22} do not propagate, therefore $\Omega_{22} = 0$.
- The case $K_p = 1$ corresponds to the biaxial compression case in Table 1. In the absence of stress difference between directions 1 and 2, the rate of damage components Ω_{11} and Ω_{22} is zero. The minimum stress is $\sigma_{33} = 0$. Vertical crack planes perpendicular to direction 3 (Ω_{33}) are generated by the differential stress along direction 3.

For $K_p < 1$, increasing the confinement σ_{22} reduces the total deviatoric stress $\sigma_{11} - \sigma_{22}$ applied to the sample during the biaxial compression test: it is therefore expected that the accumulated horizontal damage component Ω_{22} will decrease when K_p increases. It is worth noticing however that for $0 \leq K_p \leq 0.2$, Ω_{22} increases. This result can be explained from the way boundary conditions are applied during the tests: the confining stress for $K_p = 0$ is less than that for $K_p = 0.2$. Damage initiates at higher deviatoric stress for $K_p = 0$ (Figure 5). As a result, the damage that can be generated during the later loading stages is less for $K_p = 0$ than for $K_p = 0.2$, which explains why the final value of Ω_{22} is less for $K_p = 0$ than for $K_p = 0.2$. For $K_p = 0$, we have $\sigma_{22} = \sigma_{33} = 0$ and therefore, by symmetry, $\Omega_{22} = \Omega_{33}$. Under states of stress such that $\sigma_{11} = \sigma_{22}$, cracks open

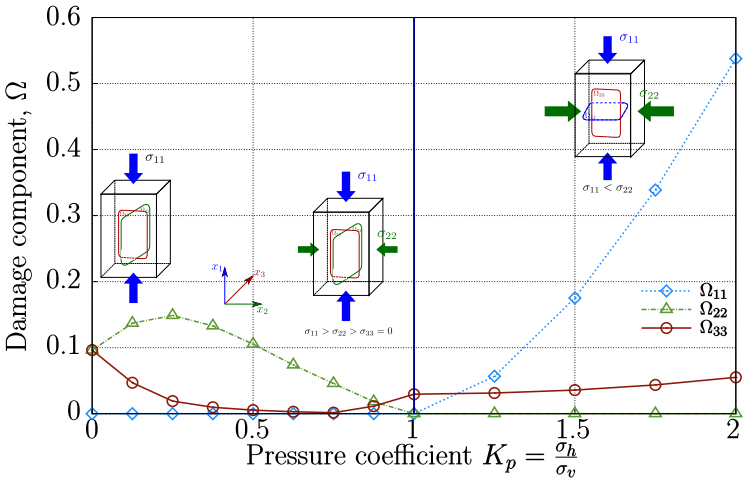

Fig. 4 Damage generation with various horizontal loads in biaxial compression tests ($\sigma_{11} = \sigma_v$; $\sigma_{22} = \sigma_h$; $\sigma_{33} = 0$). When $K_p < 1$, cracks propagate within vertical planes (perpendicular to the smaller compression stress). The corresponding damage propagates in the directions perpendicular to the crack planes: horizontal damage components Ω_{22} and Ω_{33} correspond to vertical cracks. When $K_p > 1$, deviatoric stresses $\sigma_{22} - \sigma_{33}$ and $\sigma_{11} - \sigma_{33}$ produce damage in both directions 2 and 1, i.e. both vertical and horizontal cracks.

only in planes perpendicular to direction 3 (i.e. only Ω_{33} increases). In other stress conditions, energy is released to open cracks in different directions, which explains why the variations of Ω_{33} with K_p are not linear. Stress-strain curves obtained for $K_p < 1$ are shown in Figure 5. Simulations performed with $K_p > 1$ provide only one stress-strain curve: the final stress point for each simulation is indicated in Figure 6.

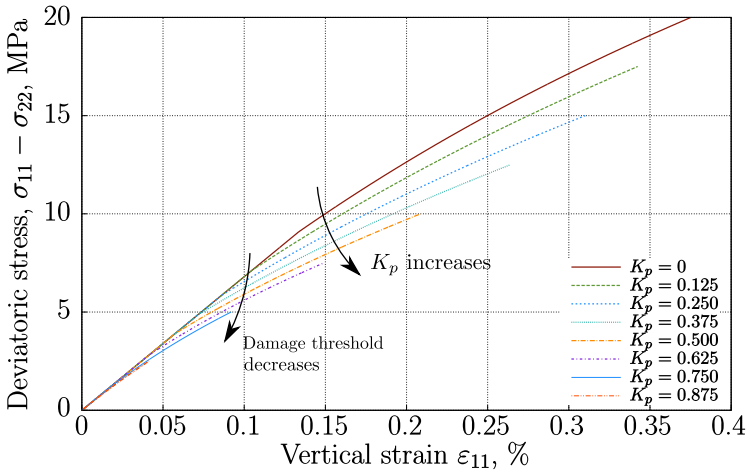

Fig. 5 Stress-strain curves for simulations with $K_p < 1$: the damage threshold decreases when K_p increases.

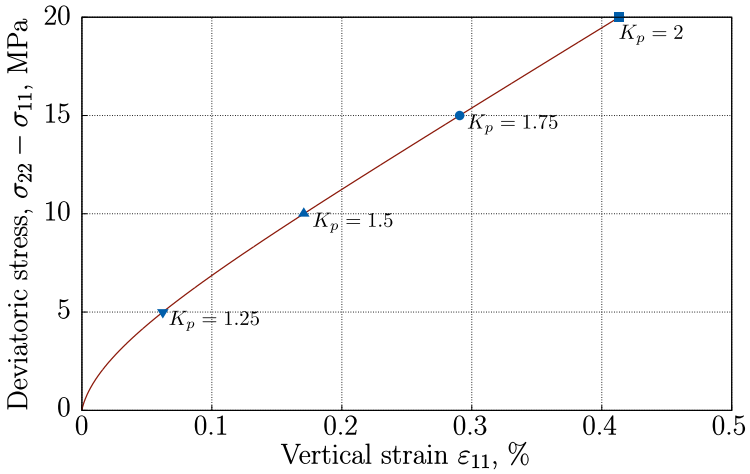

Fig. 6 Stress-strain curves for simulations with $K_p > 1$: all simulations represent the same stress path; lower K_p provide the state of stress at an earlier stage of the deviatoric compression loading stage.

4 Microscopic and macroscopic damage rotation

4.1 Continuum Mechanics representation of damage rotation

"Damage rotation" refers to a change of damage principal directions, i.e. to a configuration in which shear damage components (off the tensor diagonal) are non-zero. The principal directions of damage produced during a pure shear test are oriented at an angle of 45^o to the shear planes. Damage can be represented by an equivalent macroscopic crack oriented at an angle of 45^o to the shear planes; the volume fraction of that equivalent macroscopic crack is equal to the volume fraction of microscopic shear cracks of similar orientation, which defines a damage eigenvalue (Figure 7). Note that damage provides the average orientation of microscopic cracks. At the microscopic scale, shear cracks in rocks are composite flaws: pairs of tensile cracks (Chan et al, 1996; Swoboda and Yang, 1999) and wing cracks (Bobet and Einstein, 1998) were observed at the tip of growing shear cracks. Flaw linkage through wing cracks was explained in (Steif, 1984; Lauterbach and Gross, 1998; Willemse and Pollard, 1998; Dyskin et al, 1999). At the macroscopic scale, damage produced by shear stress (inclined crack plane) has the same effect on deformation and stiffness as damage produced by stress difference (two perpendicular crack planes). A change of coordinate system allows one to capture damage under compression with the DSID model (Ortiz, 1985). Figure 7 shows that different states of stress can lead to the same state of damage.

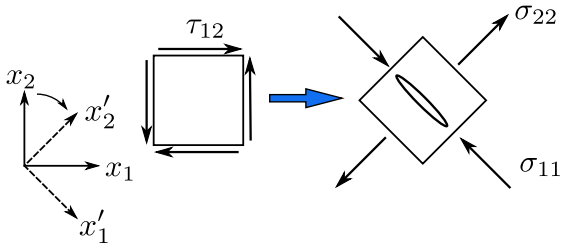

Fig. 7 Macroscopic crack propagation driven by macroscopic differential stress, as a result of the propagation and linkage of microscopic tensile cracks.

4.2 Stress path-dependence of damage rotation

The example presented below illustrates the stress-path dependence of damage. Let us consider a material element subject to: (1) a pure shear stress of $\sigma_{12} = 60$ MPa, followed by a uniaxial stress of $\sigma_{11} = 100$ MPa applied under a lateral confinement of $\sigma_{22} = \sigma_{33} = 10$ MPa; (2) a uniaxial stress of $\sigma_{11} = 100$ MPa applied under a lateral confinement of $\sigma_{22} = \sigma_{33} = 10$ MPa, followed by a pure shear stress of $\sigma_{12} = 60$ MPa. For paths (1) and (2), the evolutions of stress are illustrated on Mohr's circles and on material elements, in Figures 8(a) and 9(a) respectively. The damage tensor is noted as

$$[\Omega] = \begin{bmatrix} \Omega_{11} & \Omega_{12} & \Omega_{13} \\ \Omega_{12} & \Omega_{22} & \Omega_{23} \\ \Omega_{13} & \Omega_{23} & \Omega_{33} \end{bmatrix} \tag{15}$$

Numerical simulations performed with the DSID model provide the following results:

– Path (1): damage produced by shear stress ($\Omega^{(shear)}$), accumulated damage produced by shear stress followed by triaxial compression ($\Omega^{(comp)}$)

$$[\Omega^{(shear)}] = 10^{-4}\times\begin{bmatrix} 75 & -75 & 0 \\ -75 & 75 & 0 \\ 0 & 0 & 1.90 \end{bmatrix} \qquad [\Omega^{(comp)}] = 10^{-4}\times\begin{bmatrix} 163 & -227 & 0 \\ -227 & 338 & 0 \\ 0 & 0 & 65 \end{bmatrix} \tag{16}$$

– Path (2): damage produced by triaxial compression ($\Omega^{(comp)}$), accumulated damage produced by triaxial compression followed by shear stress ($\Omega^{(shear)}$)

$$[\Omega^{(comp)}] = 10^{-4}\times\begin{bmatrix} 0 & 0 & 0 \\ 0 & 35 & 0 \\ 0 & 0 & 35 \end{bmatrix} \qquad [\Omega^{(shear)}] = 10^{-4}\times\begin{bmatrix} 35 & -86 & 0 \\ -86 & 265 & 0 \\ 0 & 0 & 267 \end{bmatrix} \tag{17}$$

The damage tensor is symmetric, therefore, normal and tangential damage components are related by the equation of a circle - like for the stress tensor (Crossno et al, 2005). In two dimensions,

$$\begin{aligned} R^2 &= (\Omega_{ii} - C)^2 + (\Omega_{12})^2 \\ R^2 &= \left(\frac{\Omega_{11} - \Omega_{22}}{2}\right)^2 + (\Omega_{12})^2 \\ C &= \frac{\Omega_{11} + \Omega_{22}}{2} \end{aligned} \tag{18}$$

The corresponding damage Mohr's circles are plotted in Figures 8(b) and 9(b). Pure shear stress (step 1 in stress path 1, Figure 8(a)), produces shear and normal damage of the same magnitude ($\Omega_{11} = \Omega_{22} = |\Omega_{12}|$), as illustrated in Figure 8(b)). A triaxial compression (step 1 in stress path 2, Figure 9(a)) induces damage Ω_{22} only (cracks normal to the direction of the major principal stress). The differential stress that builds up during the first loading step is higher for stress path 1 (pure

shear applied first) than stress path 2 (triaxial compression applied first). More damage is accumulated at the end of the first loading step of path 1 than at the end of the first loading step of stress path 2. During step 1, the material element undergoes more hardening during the stress path 1 than during the stress path 2. As a result, the principal directions of damage rotate less during the second step of stress path 1 than during the second step of stress path 2 (Figures 8(b) and 9(b)). During the triaxial compression phase of path 1, the macro-crack propagates and rotates counter-clockwise (Figure8(b)). During the shearing phase of stress path 2, the macro-crack grows and rotates clockwise (Figure9(b)). This elementary analysis proves that damage rotation is influenced by the loading sequence, due to the non-linear nature of the DSID model.

5 Stress and damage anisotropy around pressurized cavities

We conducted a Finite Element (FE) analysis in order to characterize the development of shear damage around a circular cavity subjected to pressurization. Simulations were performed in three dimensions. The domain adopted for this study was a thin parallelepiped containing a circular hole, as shown in Figure 10. The ratio width-length was chosen so as to be close to a state of plane strain. The geometric shape of the domain used for this FE analysis allows one to impose an anisotropic state of stress around the circular cavity, which enables one to study shear damage. In the first loading stage, the same confining stress ($\sigma_0 = \sigma_{11} = \sigma_{22} = 10$ MPa) was applied normal to the external boundaries and normal to the cavity walls. In the second loading phase, the confining stress was maintained in the far field (on the external boundaries), and a variation of pressure was applied at the

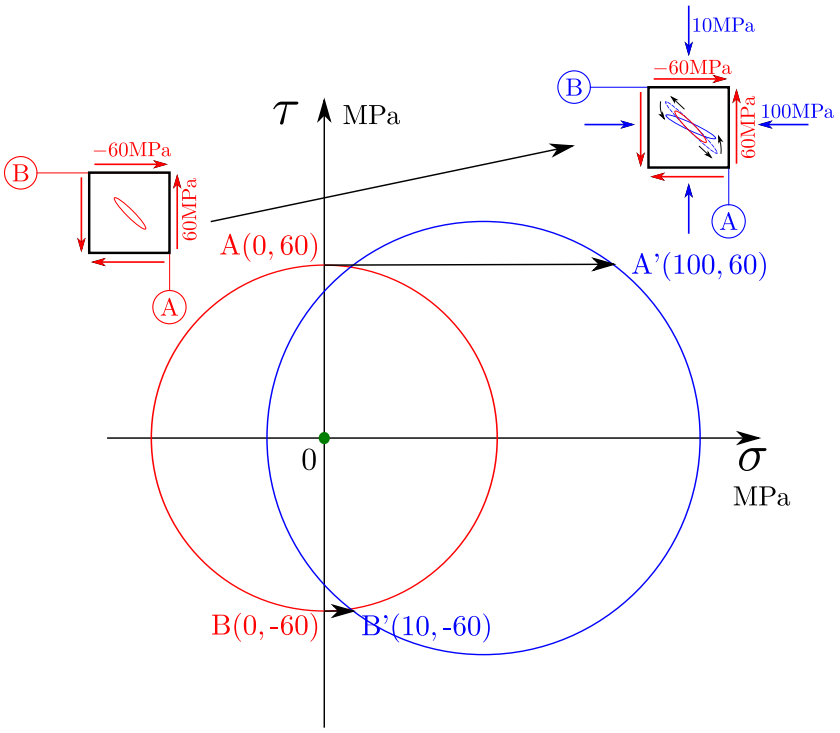

(a) Stress path 1: shear, triaxial compression

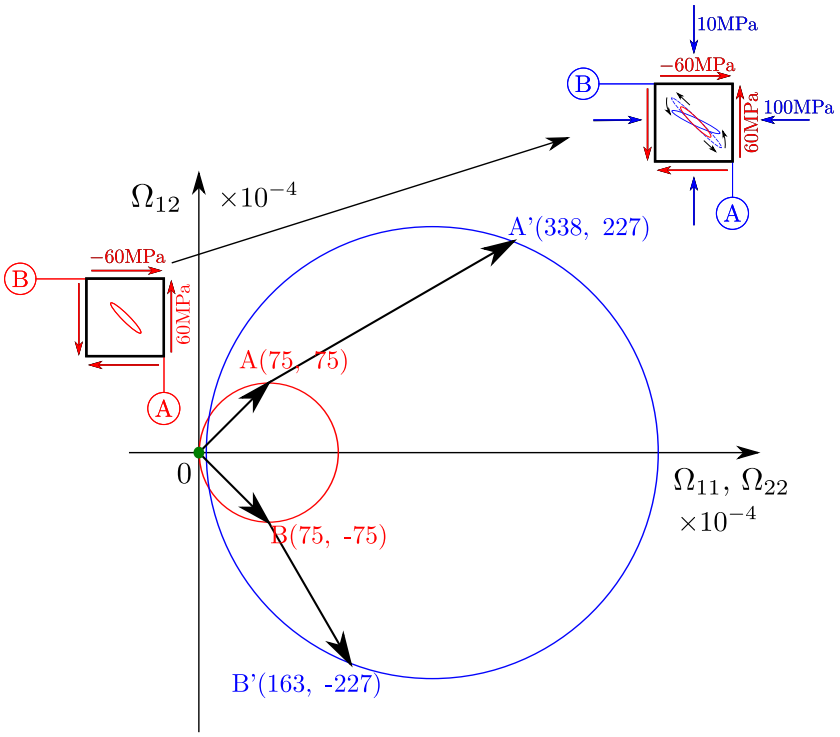

(b) Damage evolution, path 1

Fig. 8 Evolution of stress and damage at the material element level for stress path 1: pure shear followed by triaxial compression. Stress (a) and damage (b) components in plane (x_1; x_2) are represented by using Mohr's circles.

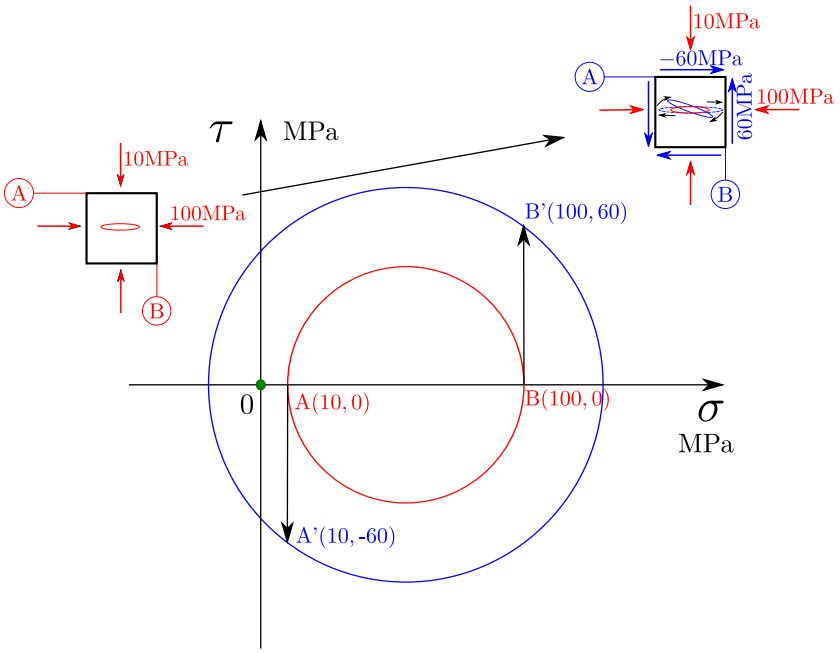

(a) Stress path 2: triaxial compression, shear

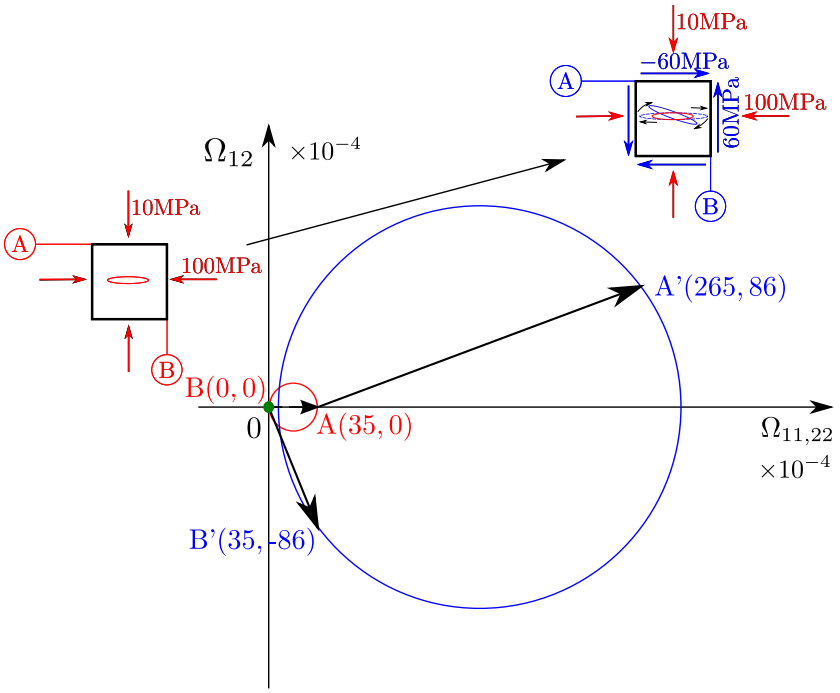

(b) Damage evolution, path 2

Fig. 9 Evolution of stress and damage at the material element level for stress path 2: triaxial compression followed by pure shear. Stress (a) and damage (b) components in plane $(x_1; x_2)$ are represented by using Mohr's circles.

cavity wall: $\Delta\sigma_p = 20; 30; 40; 50; 70; 100$ MPa. Constitutive parameters used in the DSID model are listed in Table 2. Former studies (Halm and Dragon, 2002; Shao et al, 2005) indicate that this set of parameters is suitable for granite.

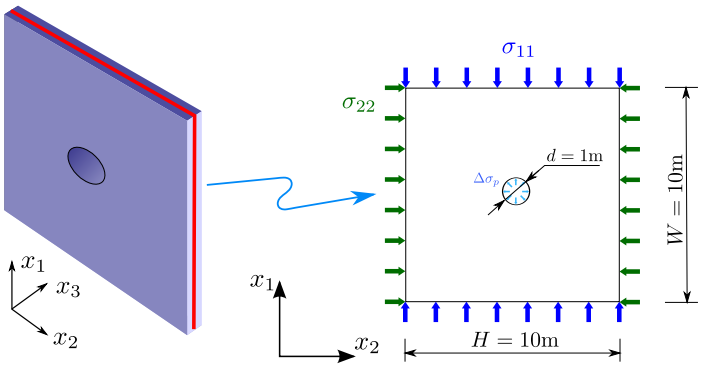

Fig. 10 Domain of study in the Finite Element Analysis: simulations were performed in three dimensions, and analyses were restricted to a central cross-section of the domain, which can be considered in a state of plane strain.

Table 2 Damage parameters for granite (Halm and Dragon, 2002; Shao et al, 2005).

Free energy				Damage function		
a_1	a_2	a_3	a_4	C_0	C_1	α (-)
GPa^{-1}	GPa^{-1}	GPa^{-1}	GPa^{-1}	MPa	MPa	-
1.26×10^{-4}	3.94×10^{-2}	-1.26×10^{-3}	2.51×10^{-4}	0.11	2.2	0.231

According to the theory of elasticity (Jaeger et al, 2007), the plane strain distribution of stress around a circular hole of radius R, embedded in an infinite medium subjected to a uniform internal pressure σ_p, and an isotropic far field

stress σ_0, is given by

$$\sigma_{\theta\theta} = \sigma_0 \left[1 + \left(\frac{R}{r}\right)^2\right] - \left(\frac{R}{r}\right)^2 \sigma_p \tag{19}$$

$$\sigma_{rr} = \sigma_0 \left[1 - \left(\frac{R}{r}\right)^2\right] + \left(\frac{R}{r}\right)^2 \sigma_p \tag{20}$$

Figure 11 shows the radial distribution of stress along the vertical direction, after a pressurization ranging between 20 MPa and 100 MPa, for an initial confining pressure $\sigma_0 = \sigma_{11} = \sigma_{22} = 10$MPa. The stress distribution predicted with the DSID model matches the elastic solution for pressure differences up to 50 MPa. Above this value, the stress magnitude at the wall decreases due to material softening.

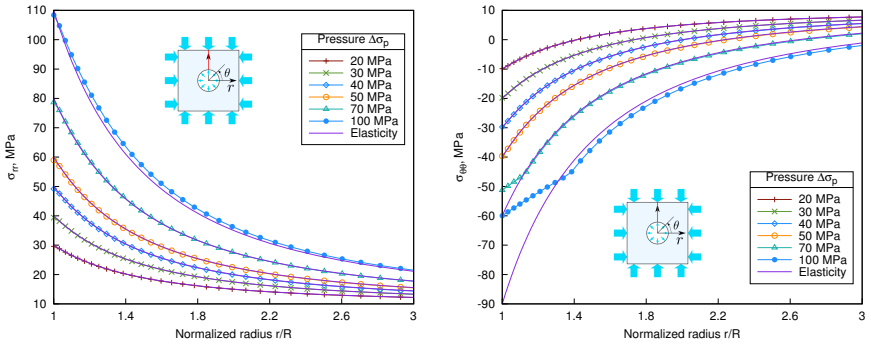

(a) Radial stess (σ_{rr}) (b) Hoop stress ($\sigma_{\theta\theta}$)

Fig. 11 Radial distribution of stress, after pressurization under a confining pressure of $\sigma_0 = \sigma_{11} = \sigma_{22} = 10$ MPa ($r = 0.5 \sim 1$ m, $\theta = \frac{\pi}{2}$, $R = 0.5$ m is the radius of the cavity). Comparison of the numerical predictions (with the DSID model) with the analytical solution (in elasticity).

Figures 12 and 13 show the final distribution of stress and damage for $\sigma_0 = \sigma_{11} = \sigma_{22} = 10$ MPa and $\Delta\sigma_p = 100$ MPa. Stress calculated with the DSID model was normalized by that obtained in linear elasticity for the same Young's modulus,

Poisson's ratio and loading conditions. Note that at the transition between tension and compression (when the elastic stress approaches zero), the stress ratio tends to infinity. In order to represent the results in a map with the same stress scale, we represented this transition zone in black in Figures 12 and 13. The main conclusions are the following:

(i) Damage propagates as a result of the stress differences imposed in compression. FE results are conform to the numerical results obtained for biaxial compression tests in Section 3: vertical (respectively, horizontal) damage propagates in parts of the rock mass where vertical stress is the minimum (respectively, maximum) principal stress, i.e. at the crown (respectively, at the side walls).

(ii) Correspondingly, stresses drop where damage is produced. In the zone of transition between tension and compression, stress concentrations are observed, whereas far field stresses calculated with the DSID model are equal to the elastic stresses.

(iii) Crack propagation releases the orthoradial (ie. tangential) stress, which redistributes principal stress differences in the immediate vicinity of the cavity. As a result, shear stress (σ_{12}) is less in a damaged rock mass than in an elastic rock mass. In the elastic zone away from the cavity, the shear stress calculated with the damage model exceeds the one that would be obtained with a linear elastic model, because of rock softening around the cavity.

(iv) Maximum principal stresses (in compression) are orthoradial, which results in the propagation of cracks perpendicular to the cavity wall. As a result, vertical cracks are observed at the crown (Figure 13(a)), and horizontal cracks develop at the side walls (Figure 13(b)).

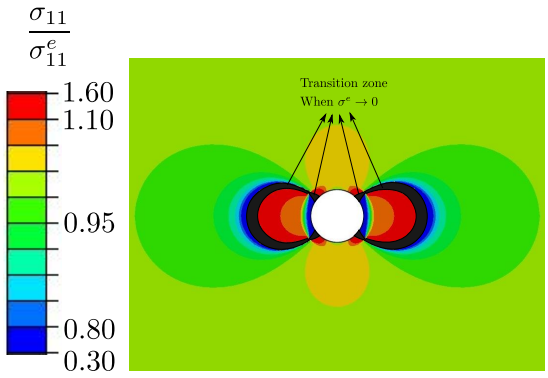

(a) Vertical stress (σ_{11}, Pa)

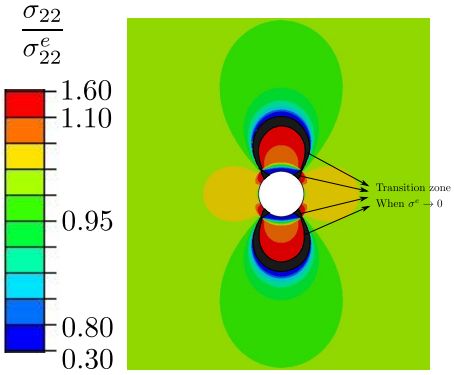

(b) Horizontal stress (σ_{22}, Pa)

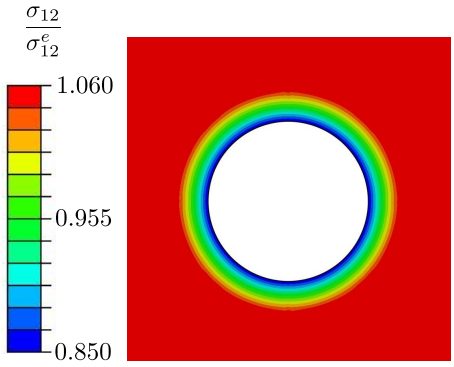

(c) Shear stress (σ_{12}, Pa)

Fig. 12 Normalized stress distribution after a pressurization of $\Delta\sigma_p = 100$ MPa in a rock mass subjected to a confining pressure of $\sigma_0 = 10$ MPa in the far field.

Figure 13 shows that vertical cracks propagate at the crown, and that horizontal cracks propagate at the sidewalls, i.e. that cracks are oriented perpendicular to the cavity wall, which corresponds to orthoradial damage. As a result, the impact of damage on the distribution of radial stress is negligible. These simulations reveal the presence of cracks that propagate under the influence of compressive stress difference. Stress elements at crown are almost in a state of pure compression in the radial direction and in a state of pure tension in the orthoradial (ie. tangential) direction.

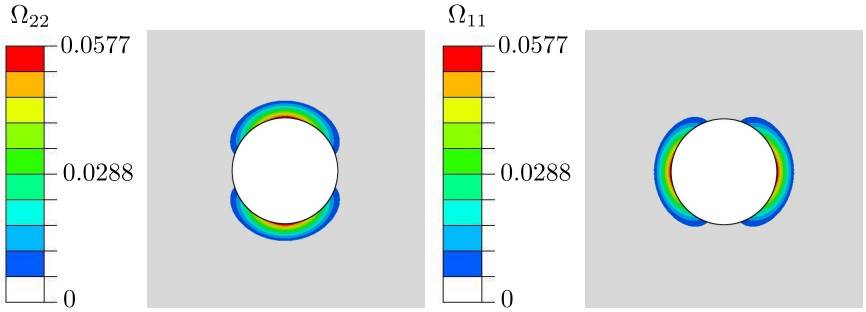

(a) Vertical macro-cracks (Ω_{22})

(b) Horizontal macro-cracks (Ω_{11})

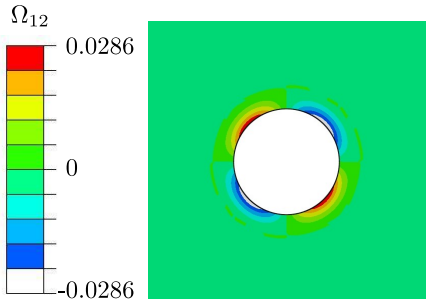

(c) Shear damage (Ω_{12})

Fig. 13 Damage distribution after a pressurization of $\Delta\sigma_p = 100$ MPa in a rock mass subjected to a confining pressure of $\sigma_0 = 10$ MPa in the far field. Note that by definition, damage eigenvalues cannot be negative, but components of the damage tensor off the diagonal can be negative.

6 Effect of stress path on damage anisotropy around cavities

We now perform a sensitivity analysis in order study the influence of the loading sequence on stress and damage anisotropy, and to identify the stress conditions in which the principal directions of damage are expected to rotate. We simulated the following loading sequences:

- Pressurization under anisotropic far field stress (Sequence 0): (1) isotropic far field stress and uniform stress at the cavity wall ($\sigma_p = \sigma_0 = 50$ MPa); (2) additional vertical far field stress ($\Delta\sigma_{11} = 20$ MPa, 50 MPa); (3) pressurization ($\Delta\sigma_p = 50$ MPa).
- Depressurization under anisotropic far field stress (Sequence 1): (1) isotropic far field stress and uniform stress at the cavity wall ($\sigma_p = \sigma_0 =$50 MPa); (2) additional vertical far field stress ($\Delta\sigma_{11} = 30$ MPa; 50 MPa); (3) depressurization ($\Delta\sigma_p = -\sigma_0$).
- Depressurized cavity subject to vertical far field stress (Sequence 2): (1) isotropic far field stress and uniform stress at the cavity wall ($\sigma_p = \sigma_0 =$50 MPa); (2) depressurization ($\Delta\sigma_p = -\sigma_0$); (3) additional vertical far field stress ($\Delta\sigma_{11} =$ 30 MPa; 50 MPa).

Table 3 summarizes all the simulations conducted in this study of stress paths effects.

The distribution of elastic stress around a circular cavity subject to an isotropic far-field stress σ_0 and to a uniform internal pressure $\sigma_p + \Delta\sigma_p$ at the wall is given in equation 19. The distribution of elastic stress around a circular cavity subject to a biaxial far-field stress ($p = \sigma_0 + \Delta\sigma_{11}$; $Kp = \sigma_0$) is given in Jaeger et al (2007). The superposition of the two provides the distribution of stress expected around

Table 3 Simulation plan for the sensitivity analysis on stress path's effects.

Sequence	Test	Step 1			Step 2			Step 3		
		σ_{11}	σ_{22}	σ_p	$\Delta\sigma_{11}$	$\Delta\sigma_{22}$	$\Delta\sigma_p$	$\Delta\sigma_{11}$	$\Delta\sigma_{22}$	$\Delta\sigma_p$
0	Test 1	50	50	50	20	0	0	0	0	50
	Test 2	50	50	50	50	0	0	0	0	50
1	Test 3	50	50	50	30	0	0	0	0	-50
	Test 4	50	50	50	50	0	0	0	0	-50
2	Test 5	50	50	50	0	0	-50	30	0	0
	Test 6	50	50	50	0	0	-50	50	0	0

the cavity before damage occurs:

$$\begin{aligned} \sigma_{\theta\theta} &= 2\sigma_0 + \Delta\sigma_{11} + 2\Delta\sigma_{11}\, cos(2\theta) - (\sigma_p + \Delta\sigma_p) \\ \sigma_{rr} &= \sigma_p + \Delta\sigma_p \\ \sigma_{r\theta} &= 0 \end{aligned} \tag{21}$$

In the following, we analyze the predictions of stress and damage obtained with the DSID model for a rock characterized by a zero tensile strength and a non-zero compressive strength. The damage criteria employed in the DSID model involve phenomenological parameters (C_0 and C_1). Although qualitative, the following interpretations are aimed to explain how the DSID model can be used to infer stress history from fracture patterns observed around cavities.

6.1 Pressurization under anisotropic far field stress

At a given point of the cavity wall, σ_{rr} and $\sigma_{\theta\theta}$ are principal stresses (Equation 21). In the DSID model, damage occurs when the difference between two principal stresses exceeds a certain threshold. If the far-field stress is isotropic, $\Delta\sigma_{11} = 0$

and $\sigma_{\theta\theta} - \sigma_{rr} = 2(\sigma_0 - \sigma_p - \Delta\sigma_p)$. The maximum difference between principal stresses does not depend on the location of the material point at the cavity wall, therefore the damage threshold is reached simultaneously at all material points of the cavity wall. If the internal pressure exceeds the far field stress, $\sigma_{\theta\theta} < \sigma_{rr}$, and cracks propagate in the direction normal to the cavity wall, as illustrated in Figure 13. If an additional vertical stress is applied in the far field before pressurization, the difference between principal stresses becomes dependent on the orientation of the stress element considered: $\sigma_{\theta\theta} - \sigma_{rr} = 2(\sigma_0 - \sigma_p - \Delta\sigma_p) + \Delta\sigma_{11} + 2\Delta\sigma_{11}\, cos(2\theta)$. In the parametric study presented here, $\sigma_0 = \sigma_p$, hence $\sigma_{\theta\theta} - \sigma_{rr} = -2\Delta\sigma_p + \Delta\sigma_{11}(1 + 2cos(2\theta))$.

If one assumes that rock tensile strength is zero, cracks perpendicular to the cavity wall will propagate for $\sigma_{\theta\theta} - \sigma_{rr} \leq 0$. At the end of the vertical loading stage and before pressurization ($\Delta\sigma_p = 0$), tensile cracks are generated for $\pi/3 < \theta < 2\pi/3$ (at the top crown) and $4\pi/3 < \theta < 5\pi/3$ (at the crown bottom). Figure 14 shows that pressurization enlarges the zone of potential tensile damage to a zone such that $cos(2\theta) < \frac{\Delta\sigma_p}{\Delta\sigma_{11}} - \frac{1}{2}$. The DSID model allows predicting the propagation of these tensile cracks: at the crown, the direction of damage is orthogonal to the wall ($\Omega_{22} > \Omega_{11}$).

Noting σ_c the compressive strength of the rock, compressive cracks parallel to the cavity wall propagate for $\sigma_{\theta\theta} - \sigma_{rr} > \sigma_c$. If no damage is created during the vertical compression phase, then the compressive damage zone extends from $\theta = -cos^{-1}\left(\frac{\sigma_c + 2\Delta\sigma_p}{2\Delta\sigma_{11}}\right)$ to $\theta = +cos^{-1}\left(\frac{\sigma_c + 2\Delta\sigma_p}{2\Delta\sigma_{11}}\right)$, and from $\theta = \pi - cos^{-1}\left(\frac{\sigma_c + 2\Delta\sigma_p}{2\Delta\sigma_{11}}\right)$ to $\theta = \pi + cos^{-1}\left(\frac{\sigma_c + 2\Delta\sigma_p}{2\Delta\sigma_{11}}\right)$ (i.e., at the sidewalls). For $\Delta\sigma_{11} = 20$ MPa (Figures 14.a and 14.c), damage propagates only at the crown. For $\Delta\sigma_{11} = 50$ MPa (Figures 14.b and 14.d), damage propagates also at the side walls, due to stress

redistribution. Note that when the last pressurization loading stage is replaced by a pressurization such that $\Delta\sigma_p = -\sigma_p = -\sigma_0$ (not shown here for the sake of brevity), we have: $\sigma_{\theta\theta} - \sigma_{rr} = 2\sigma_0 + \Delta\sigma_{11}(1 + 2cos(2\theta))$. Compression damage propagates if $\sigma_{\theta\theta} - \sigma_{rr} > \sigma_c$, i.e. for $cos(2\theta) \geq \frac{\sigma_c - 2\sigma_0}{2\Delta\sigma_{11}} - \frac{1}{2}$. The distribution of damage is symmetric about the horizontal axis, and compression damage spreads at the sidewalls.

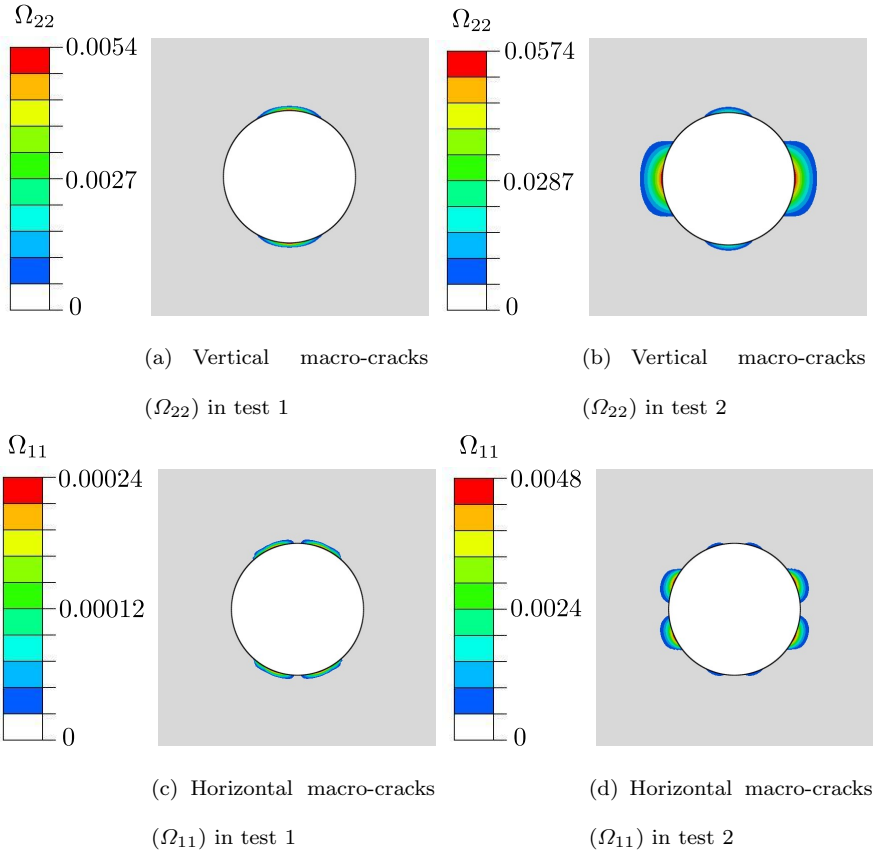

(a) Vertical macro-cracks (Ω_{22}) in test 1

(b) Vertical macro-cracks (Ω_{22}) in test 2

(c) Horizontal macro-cracks (Ω_{11}) in test 1

(d) Horizontal macro-cracks (Ω_{11}) in test 2

Fig. 14 Damage distribution after application of a vertical far field stress $\Delta\sigma_{11}$ followed by a pressurization, under a confining pressure of $\sigma_0 = 50$ MPa (Sequence 0).

6.2 Depressurization of cavities in isotropic and anisotropic stress conditions

Under the same initial stress and far field stress conditions, the distribution of damage around a depressurized cavity subject to a vertical far field stress (i.e. a cavity subject to depressurization before $\Delta\sigma_{11}$ is applied) is similar to that around a cavity subject to depressurization under anisotropic far field stress (i.e. a cavity subject to depressurization after $\Delta\sigma_{11}$ is applied). As an example, Figure 15 shows the damage zone around a depressurized cavity subject to $\Delta\sigma_{11} = 50$ MPa (Sequence 2). Figure 16(b) shows the variations of the major damage eigenvalue along axes oriented by 45° to the horizontal. In Figure 16(a), the radial distribution of the damage components along axes oriented by 45° to the horizontal indicates that the position of maximum density of vertical cracks (Ω_{22}) is located at the wall of the cavity when the vertical load is applied before the depressurization (Sequence 1), and inside the rock mass when the vertical load is applied after the depressurization (Sequence 2). Differences in the proportions between damage components result in different principal directions of the damage tensor. In particular, Figure 16(a) shows that the departure from the horizontal is larger when $\Delta\sigma_{11}$ is applied after depressurization (Sequence 2) than when $\Delta\sigma_{11}$ is applied before depressurization (Sequence 1).

7 Conclusion

We used the Differential Stress Induced Damage (DSID) model to predict anisotropic crack propagation under tensile, deviatoric and shear stress. The damage variable is similar to a crack density tensor. Damage represents three equivalent macroscopic cracks (defined at the scale of the Representative Elementary Volume):

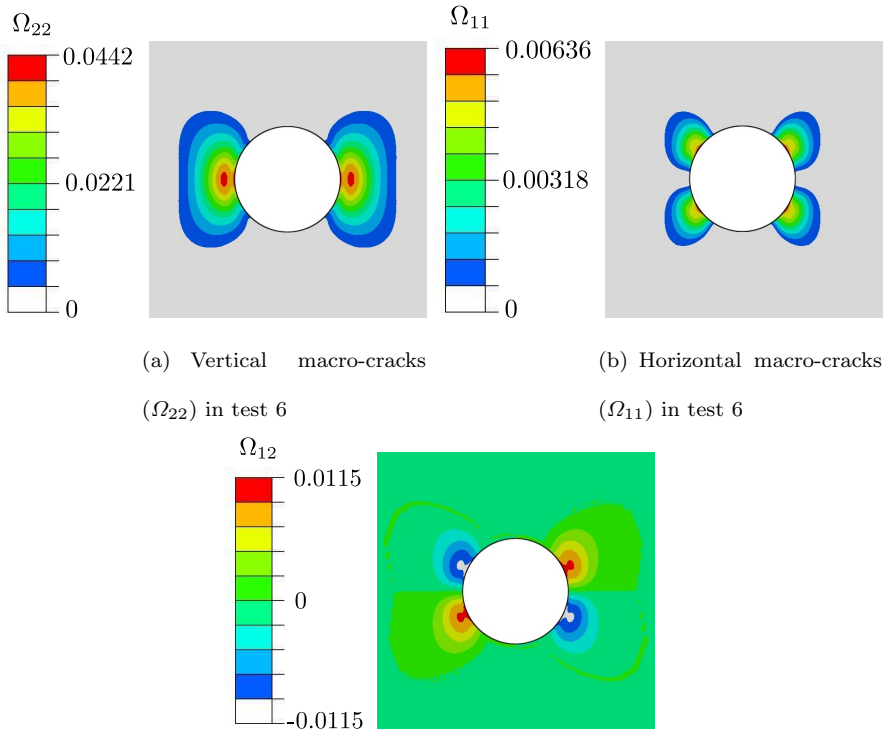

(a) Vertical macro-cracks (Ω_{22}) in test 6

(b) Horizontal macro-cracks (Ω_{11}) in test 6

(c) Shear damage (Ω_{12}) in test 6

Fig. 15 Depressurization followed by the application of a vertical far field stress $\Delta\sigma_{11} = 50$ MPa, under a confining pressure of $\sigma_0 = 50$ MPa (test 6 in sequence 2). Damage distribution.

damage eigenvectors are orthogonal to the macroscopic crack planes, and damage eigenvalues are the volume fractions of these macroscopic cracks. The solid skeleton free energy is a polynomial of order two in stress, and order one in damage. In contrast to existing damage models proposed for geomaterials, flow rules are derived with the energy release rate work-conjugate to damage, which is thermodynamically consistent. The damage criterion is similar to the Drucker-Prager yield function, except that the criterion is expressed in terms of damage energy release rate projected in the positive space, in order to distinguish between tension and compression damage thresholds. Non-elastic deformation due to damage

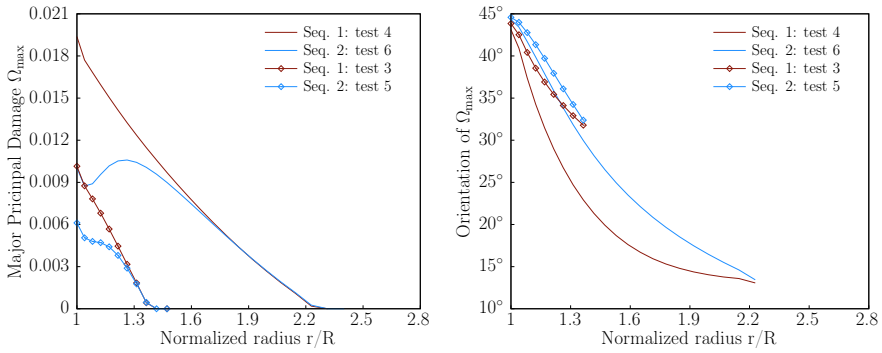

(a) Principal damage (b) Damage direction

Fig. 16 Application of a vertical far field stress followed by a depressurization (Sequence 1) and depressurization followed by the application of a vertical far field stress (Sequence 2), under a confining pressure of $\sigma_0 = 50$ MPa. Plots indicate the intensity and orientation of damage eigenvalues at material points located on radial axes oriented by $\theta = 45°$ to the horizontal.

is computed with an associate flow rule in order to ensure that damage propagates in planes that are normal to the minor principal stress (tension negative).

We simulated biaxial compression tests at the material point level. We verified that: (1) three dimensional states of damage can be obtained for three dimensional states of stress; (2) no damage propagates under isotropic compression; (3) crack planes propagate in the direction parallel to major compression stress; (4) damage propagation hardens the material; (5) stiffness and deformation anisotropy result from the anisotropy of damage. There is no one-to-one relationship between stress and damage, i.e., a given state of damage can be produced by different stress paths. However, we demonstrated the effect of the loading sequence on a two-step simulation (a shear loading phase and a compression loading phase). From stress and damage Mohr circles, it is apparent that the current state of stress and damage can be used to track the effect of stress history on damage rotation.

We finally conducted a sensitivity analysis with the Finite Element Method, in order to explore the stress conditions in which damage is expected to rotate around a circular cavity subjected to pressurization or depressurization. Simulation results showed that: (1) before damage initiation, the DSID model matches the analytical solution of stress distribution obtained within the theory of elasticity; (2) the DSID model can predict the extent of the tensile damage zone at the crown, and that of the compressive damage zone at the sidewalls; (3) damage generated during a vertical far field compression followed by a depressurization of the cavity is more intense that that generated during a depressurization of the cavity followed by a vertical far-field compression.

Acknowledgements This study was conducted at the Georgia Institute of Technology, as part of a research program on Finite Element Modeling of Hydraulic Fracturing. Funding was provided by ConocoPhillips, Houston, Texas.

A Notation - List of Parameters

Symbol	Name	Dimensions	SI Units
$\boldsymbol{\Omega}$	Damage tensor	$M^0L^0T^0$	-
N	Number of cracks	$M^0L^0T^0$	-
d_k	Volumetric fraction of the cracks	$M^0L^0T^0$	-
$\mathbf{n}_k$	Normal direction of the kth crack	$M^0L^0T^0$	-
r_i	Radius of the ith crack plane	$M^0L^1T^0$	mm
e_i	Thickness of the ith crack plane	$M^0L^1T^0$	mm
$\boldsymbol{\varepsilon}$	Total strain	$M^0L^0T^0$	-
$\boldsymbol{\varepsilon}^{el}$	Pure elastic strain	$M^0L^0T^0$	-
$\boldsymbol{\varepsilon}^{ed}$	Elasto-damage strain	$M^0L^0T^0$	-
$\boldsymbol{\varepsilon}^{id}$	Irreversible strain	$M^0L^0T^0$	-
$\boldsymbol{\varepsilon}^{E}$	Total elastic strain	$M^0L^0T^0$	-
$\boldsymbol{\sigma}$	Stress	$M^1L^{-1}T^{-2}$	MPa
$\mathbf{Y}$	Damage conjugated force	$M^1L^{-1}T^{-2}$	MPa
$\dot{\boldsymbol{\Omega}}$	Damage rate	$M^0L^0T^0$	-
$\boldsymbol{\varepsilon}^{el}$	Pure elastic strain	$M^0L^0T^0$	-
G_s	Gibbs free energy	$M^1L^2T^{-2}$	J
$\mathbb{S}_0$	Initial compliance tensor	$M^{-1}L^1T^2$	GPa^{-1}
a_i	Material parameters accounting for stiffness due to damage	$M^{-1}L^1T^2$	GPa^{-1}
ν_0	Initial Poisson's ratio	$M^0L^0T^0$	-
E_0	Initial Young's modulus	$M^1L^{-1}T^{-2}$	GPa
$\boldsymbol{\delta}$	2rd order identity tensor	$M^0L^0T^0$	-
f_d	Damage function	$M^1L^{-1}T^{-2}$	MPa
J^*	Second invariant of the deviatoric part of th physical damage force	$M^2L^{-2}T^{-4}$	MPa^2
I^*	first invariant of the physical damage force	$M^1L^{-1}T^{-2}$	MPa
α	Material constant to control the shape of the cone	$M^0L^0T^0$	-
C_0	Initial damage threshold	$M^1L^{-1}T^{-2}$	MPa
C_1	Damage hardening variable	$M^1L^{-1}T^{-2}$	MPa
$\mathbb{P}_1$	Projection tensor to make the damage driving force parallel to stress	$M^0L^0T^0$	-
$\mathbb{P}_2$	Projection tensor to account for the damage rate direction	$M^0L^0T^0$	-
$\sigma^{(p)}$	pth eigenstress	$M^1L^{-1}T^{-2}$	MPa
$\mathbf{n}^{(p)}$	pth principal direction	$M^0L^0T^0$	-
g_d	Damage potential	$M^1L^{-1}T^{-2}$	MPa
C_2	Hardening variable in damage potential	$M^1L^{-1}T^{-2}$	MPa

References

Abu Al-Rub RK, Kim SM (2010) Computational applications of a coupled plasticity-damage constitutive model for simulating plain concrete fracture. Engineering Fracture Mechanics 77:1577–1603

Abu Al-Rub RK, Voyiadjis GZ (2003) On the coupling of anisotropic damage and plasticity models for ductile materials. International Journal of Solids and Structures 40:2611–2643

Arson C (2009) Etude théorique et numérique de l'endommagement thermo-hydro-mécanique des milieux poreux non saturés. PhD thesis, Ecole Nationale des Ponts et Chaussées, Paris

Arson C (2012) Using a geo-mechanical damage model to assess permeability in cracked porous media: internal length parameter issues. Special Topics & Reviews in Porous Media 3:69–77

Ashby MF, Sammis CG (1990) The damage mehcanics of brittle solids in compression. Pure and Applied Geophysics 133(3):489–521

Bakhtiary E, Xu H, Arson C (2014) Probabilistic optimization of a continuum mechanics model to predict differential stress-induced damage in claystone. International Journal of Rock Mechanics & Mining Sciences

Bobet A, Einstein H (1998) Fracture coalescence in rock-type materials under uniaxial and biaxial compression. International Journal of Rock Mechanics & Mining Sciences 35(7):October

Carter NL, Hansen FD (1983) Creep of rocksalt. Tectonophysics 92(4):275–333

Chaboche JL (1992) Damage induced anisotropy: On the difficulties associated with the active/passive unilateral condition. International Journal of Damage Mechanics 1:148–171

Chaboche JL (1993) Development of continuum damage mechanics for elastic solids sustaining anisotropic and unilateral damage. International Journal of Damage Mechanics 2:311–329

Chan K, Munson D, Bodner S, Fossum A (1996) Cleavage and creep freacture of rock salt. Acta Materialia 44(9):3553–3565

Chan KS, Bodner SR, Munson DE (2001) Permeability of wipp salt during damage evolution and healing. International Journal of Damage Mechanics 10(4):347–375

Cicekli U, Voyiadjis GZ, Abu Al-Rub RK (2007) A plasticity and anisotropic damage model for plain concrete. International Journal of Plasticity 23:1874–1900

Collins IF, Houlsby GT (1997) Application of thermomechanical principles to the modelling of geotechnical materials. Proceedings: Mathematical, Physical and Engineering Sciences 453(1964):1975–2001

Crossno P, Rogers DH, Brannon RM, Coblentz D, Fredrich JT (2005) Visualization of geologic stress perturbations using mohr diagrams. IEEE Transactions on Visualization and Computer Graphics 11(5):508–518

Deng H, Nemat-Nasser S (1992) Dynamic damage evolution in brittle solids. Mechanics of Materials 14:83–103

Desmorat R (2006) Positivité de la dissipation intrinsèque d'une classe de modèles d'endommagement anisotropes non standards. Comptes Rendus Mecanique

Dyskin AV, Germanovich LN, Ustinov KB (1999) A 3-d model of wing crack growth and interaction. Engineering Fracture Mechanics 63(1):81–110

Frémond M, Nedjar B (1996) Damage, gradient of damage and principle of virtual power. International Journal of Solids and Structures 33:2294–2306

Gatmiri B, Arson C (2008) Theta-stock, a powerful tool for thermohydromechanical behaviour and damage modelling of unsaturated porous media. Computers & Geotechnics 35(8):890–915

Halm D, Dragon A (1998) An anisotropic model of damage and frictional sliding for brittle materials. Eur J Mech A/ Solids 17(3):439–460

Halm D, Dragon A (2002) Modelisation de l'endommagement par mesofissuration du granite. Revue Francaise de Genie Civi 17:21–33

Hansen N, Schreyer H (1994) A thermodynamically consistent framework for theories of elastoplasticity coupled with damage. International Journal of Solids and Structures 31(3):359–389

Hayakawa K, Murakami S (1997) Thermodynamical modeling of elastic-plastic damage and experimental validation of damage potential. International Journal of Damage Mechanics 6:333–363

Homand-Etienne F, Hoxha D, Shao JF (1998) A Continuum Damage Constitutive Law for Brittle Rocks. Computers and Geotechnics 22(2):135–151

Horii H, Nemat-Nasser S (1986) Brittle failure in compression: splitting, faulting and brittle-ductile transition. Philosophical Transactions of the Royal Society of London Series A,

MAthematical and Physical Science 319(1549):337–374

Hou Z (2003) Mechanical and hydraulic behavior of rock salt in the excavation disturbed zone around underground facilities. International Journal of Rock Mechanics & Mining Sciences 40(5):725–738

Houlsby GT, Puzrin AM (2006) Principles of hyperplasticity an approach to plasticity theory based on thermodynamic principles. London

Huang C, Subhash G, Vitton SJ (2002) A dynamic damage growth model for uniaxial compressive response of rock aggregates. Mechanics of Materials 34:267–277

Hunsche U, Hampel A (1999) Rock salt - the mechanical properties of the host rock material for a radioactive waste repository. Engineering Geology 52(3-4):271–291

Hütter M, Tervoort T (2008) Continuum damage mechanics: combining thermodynamics with a thoughtful characterization of the microstructure. Acta mechanica 201(1-4):297–312

Jaeger JC, Cook NG, Zimmerman RW (2007) Fundamentals of Rock Mechanics, fourth edition edn. Blackwell Publishing

Kachanov M (1992) Effective elastic properties of cracked solids: critical review of some basic concepts. Appl Mech Rev 45(8):304–335

Keller A, Hutter K (2011) On the thermodynamic consistency of the equivalence principle in continuum damage mechanics. Journal of the Mechanics and Physics of Solids 59(5):1115–1120

Krajcinovic D (1996) Damage Mechanics. North-Holland

Lauterbach B, Gross D (1998) Crack growth in brittle solids under compression. Mechanics of Materials 29(2):81–92

Lee J, Fenves G (1998) Plastic-damage model for cyclic loading of concrete structures. Journal of Engineering Mechanics 124:892–900

Lemaître J, Desmorat R (2005) Engineering Damage Mechanics. Ductile, creep, fatigue and brittle failure. Springer - Verlag, Berlin Heidelberg

Lubliner J, Oliver J, Oller S, Onate E (1989) A platic-damage model for concrete. International Journal of Solids and Structures 23(3):299–326

Lux KH, Eberth S (2007) Fundamentals and first application of a new healing model for rock salt. In: Proceedings and Monographs in Engineering, Water and Earth Sciences., pp

129–138

Mazars J (1986) A description of micro- and macro scale damage of concrete structures. Engineering Fracture Mechancis 25(5–6):729–737

Mazars J, Pijaudier-Cabot G (1989) Continuum damage theory - application to concrete. Journal of Engineering Mechanics 115(2):345–365

Murakami S, Kamiya K (1996) Constitutive and damage evolution equations of elastic-brittle materials based on irreversible thermodynamics. Int J Mech Sci 39:473–486

Nemat-Nasser S, Hori M (eds) (1983) Rock failure in compression, Ninth Workshop Geothermal Reservoir Engineering, Stanford University, Stanford, California

Oda M (1982) Fabric tensor for discontinuous geological materials. Soils and Foundations 22(4):96–108

Oda M (1984) Similarity rules of crack geometry in statistically homogeneous rock masses. Mechanics of Materials 3:119–129

Ortiz M (1985) A constitutive theory for the inelastic behaviour of concrete. Mech Mater 4:67–93

Pellet F, Hajdu A, Deleruyelle F, Besnus F (2005) A viscoplastic model including anisotropic damage for the time dependent behaviour of rock. International Journal for Numerical and Analytical Methods in Geomechanics 29:941–970

Raj R (1982) Creep in polycrystalline aggregates by matter transport through a liquid phase. Journal of Geophysical Research 87(B6):4731–4739

Senseny PE, Hansen FD, Russell JE, Carter NL, Handin JW (1992) Mechanical behaviour of rock salt: Phenomenology and micromechanisms. International Journal of Rock Mechanics and Mining Sciences & Geomechanics Abstracts 29(4):363–378

Shao J, Zhou H, Chau K (2005) Coupling between anisotropic damage and permeability variation in brittle rocks. International Journal for Numerical and Analytical Methods in Geomechanics 29(12):1231 – 1247

Shao JF, Chau KT, Feng XT (2006) Modeling of anisotropic damage and creep deformation in brittle rocks. International Journal of Rock Mechanics & Mining Sciences 43:582–592

Steif PS (1984) Crack extension under compressive loading. Engineering Fracture Mechanics 20(3):463–473

Swoboda G, Yang Q (1999) An energy-based damage model of geomaterials. I. Formulation and numerical results. International Journal of Solids and Structures 36(12):1719–1734

Voyiadjis GZ, Shojaei A, Li G (2011) A thermodynamic consistent damage and healing model for self healing materials. International Journal of Plasticity 27(7):1025–1044

Willemse EJ, Pollard DD (1998) On the orientation and patterns of wing cracks and solution surfaces at the tips of a sliding flaw or fault. Journal of Geophysical Research: Solid Earth (1978–2012) 103(B2):2427–2438

Xu H (2014) Theoretical and numerical modeling of anisotropic damage in rock for energy geomechancis. PhD thesis, Georgia Institute of Technology

Xu H, Arson C (2014) Anisotropic damage models for geomaterials: Theoretical and numerical challenges. International Journal of Computational Methods, Special Issue on Computational Geomechanics 11(2)

Yu H (2006) Plasticity and Geotechnics. Springer

Zhou H, Hu D, Zhang F, Shao J (2011) A thermo-plastic/viscoplastic dmage model for geomaterials. Acta Mechanica Solida Sinica 24(3):195–208

Zhou J, Shao J, Xu W (2006) Coupled modeling of damage growth and permeability variation in brittle rocks. Mechanics Research Communications 33(4):450–459

Zhu C, Arson C (2014) A thermo-mechanical damage model for rock stiffness during anisotropic crack opening and closure. Acta Geotechnica pp DOI: 10.1007/s11,440–013–0281–0 (in press)